



Making thermal sensors accurate and invisible with an anisotropic monolayer scheme

Peng Jin^a, Liujun Xu^{a,*}, Tao Jiang^b, Long Zhang^c, Jiping Huang^{a,*}

^aDepartment of Physics, State Key Laboratory of Surface Physics, and Key Laboratory of Micro and Nano Photonic Structures (MOE), Fudan University, Shanghai 200438, China

^bDepartment of Radiology, Shanghai Hospital, Naval Medical University, Shanghai 200433, China

^cKey Laboratory of Materials for High-Power Laser, Shanghai Institute of Optics and Fine Mechanics, Chinese Academy of Sciences, Shanghai 201800, China



ARTICLE INFO

Article history:

Received 4 June 2020

Revised 9 August 2020

Accepted 2 September 2020

Keywords:

Thermal sensor

Anisotropic monolayer scheme

Temperature detection

ABSTRACT

Temperature measurement is particularly significant for various fields such as industrial production and daily life, so high-performance thermal sensors become indispensable. However, bare thermal sensors inevitably distort original temperature profiles, making them inaccurate and thermally visible. Different from existing methods, here we propose an anisotropic monolayer scheme to avoid thermal sensors from distorting local and background temperature profiles, making them accurate and thermally invisible. For arbitrarily given thermal conductivities of sensors and backgrounds, we design metashells with anisotropic thermal conductivities, and perform finite-element simulations in two or three dimensions. We further experimentally fabricate a metashell with anisotropic thermal conductivity based on the effective medium theory, which confirms the feasibility of our scheme. Our results are beneficial to advance the performance of thermal detection, and may also provide guidance for other physical fields.

© 2020 Elsevier Ltd. All rights reserved.

1. Introduction

Temperature measurement has broad applications, which requires thermal sensors to have high sensitivity. However, the distortion of temperature profiles, resulting from thermal sensors themselves, cannot be avoided by only improving sensitivity. A severe problem lies in the thermal-conductivity mismatch between sensors and backgrounds. Similar problem (parametric mismatch) also occurs in some other fields, and promotes relevant researches in electromagnetism [1,2], magnetics [3], and acoustics [4–6].

To solve the above-mentioned problem in thermotics, many schemes were proposed based on neutral inclusion [7] or transformation thermotics [8]. Furthermore, a multiphysical scheme was proposed by coating a sensor with an isotropic shell [9]. Though these schemes improve the performance of thermal detection, they are also faced with problems of complex parameters and technological difficulty. For the scheme based on transformation thermotics [8], anisotropic, nonuniform, and even negative thermal conductivities are required, which makes its experimental realization extremely difficult. For the scheme based on an isotropic shell [7,9–11], local temperature profiles are still different from the

original ones, making thermal detection inaccurate. Here, “local” indicates the region occupied by a sensor. To improve accuracy, one should minimize the thickness of the isotropic shell, which, however, still cannot remove inaccuracy completely, and also results in fabrication difficulty. In this sense, to date, thermal sensors with both accuracy and invisibility are still experimentally lacking. Here, accuracy and invisibility respectively indicate that local and background temperature profiles are not distorted.

Different from existing methods [7–11], here we propose an anisotropic monolayer scheme which can accurately measure local temperature profiles without disturbing background thermal fields. It is worth noting that similar scheme has been successfully applied to design other thermal functions, such as cloaking [12–14], concentrating [13–15], and chameleon [16,17]. The present scheme is applicable for arbitrarily given thermal conductivities of backgrounds and sensors, which is confirmed by finite-element simulations in two or three dimensions. Furthermore, we experimentally fabricate a metashell with anisotropic thermal conductivity based on the effective medium theory [18–22], and the experimental results agree well with the theory and finite-element simulations.

2. Theoretical design

We start by discussing a two-dimensional system shown in Fig. 1. The system is divided by a metashell (Area II) into three

* Corresponding authors.

E-mail addresses: 13307110076@fudan.edu.cn (L. Xu), jphuang@fudan.edu.cn (J. Huang).

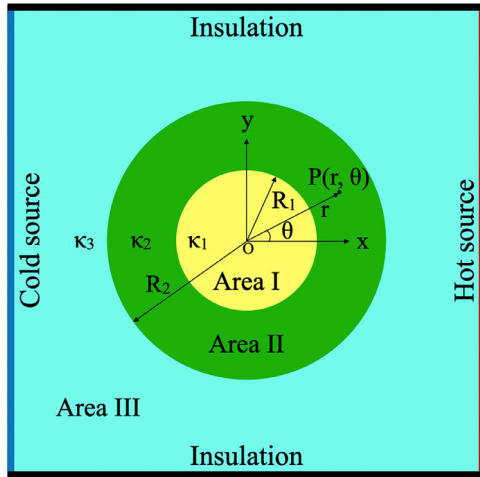


Fig. 1. Schematic diagram of the anisotropic monolayer scheme.

areas, whose thermal conductivities are κ_1 for sensor (Area I), $\kappa_2 = \begin{pmatrix} \kappa_{rr} & 0 \\ 0 & \kappa_{\theta\theta} \end{pmatrix}$ for metashell (Area II), and κ_3 for background (Area III). κ_2 is expressed in cylindrical coordinates (r, θ) , where κ_{rr} and $\kappa_{\theta\theta}$ are radial and tangential thermal conductivities, respectively. We consider the known equation describing passive heat

conduction at steady states,

$$\nabla \cdot (-\kappa \cdot \nabla T) = 0, \quad (1)$$

where κ and T are thermal conductivity and temperature, respectively.

Eq. (1) can be expanded in cylindrical coordinates as

$$\frac{1}{r} \frac{\partial}{\partial r} \left(r \kappa_{rr} \frac{\partial T}{\partial r} \right) + \frac{1}{r} \frac{\partial}{\partial \theta} \left(\kappa_{\theta\theta} \frac{\partial T}{\partial \theta} \right) = 0. \quad (2)$$

The general solution to Eq. (2) is

$$T = A_0 + B_0 \ln r + \sum_{i=1}^{\infty} [A_i \sin(i\theta) + B_i \cos(i\theta)] r^{im_1} + \sum_{j=1}^{\infty} [C_j \sin(j\theta) + D_j \cos(j\theta)] r^{jm_2}, \quad (3)$$

where $m_1 = \sqrt{\kappa_{\theta\theta}/\kappa_{rr}}$ and $m_2 = -\sqrt{\kappa_{\theta\theta}/\kappa_{rr}}$, representing anisotropy degree.

The temperature profiles of sensor (Area I), metashell (Area II), and background (Area III) are respectively denoted as T_1 , T_2 , and T_3 , which satisfy the general solution in Eq. (3). Especially, T_1 and T_3 can be given by the right side of Eq. (3) with $m_1 = 1$ and $m_2 = -1$. Boundary conditions are determined by the continuities

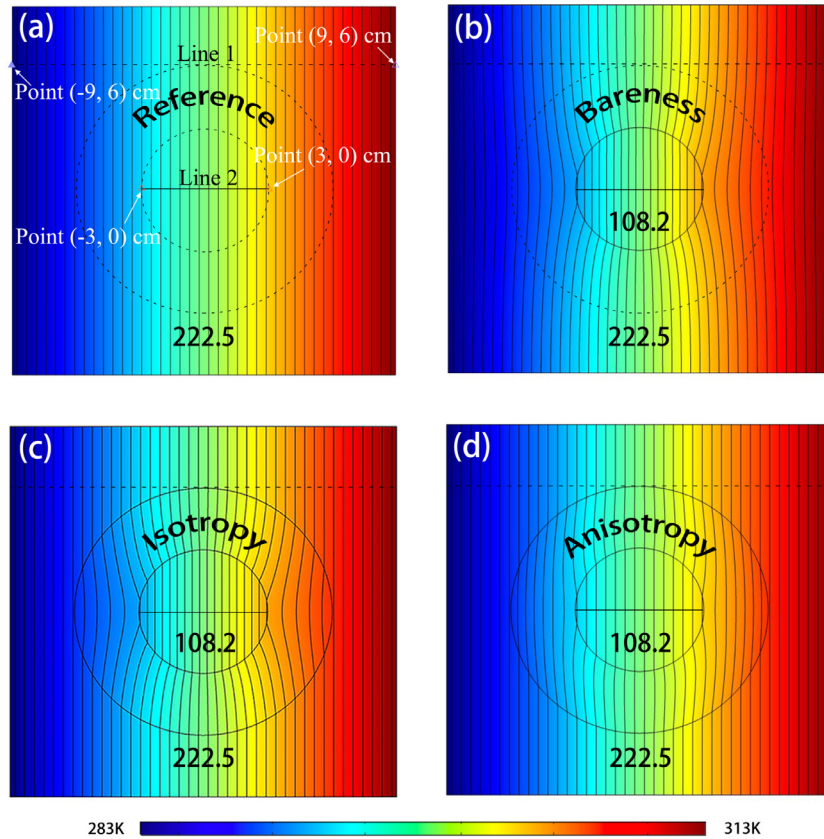


Fig. 2. Case with $\kappa_1 < \kappa_3$. The simulation box is $18 \times 18 \text{ cm}^2$, $R_1 = 3 \text{ cm}$, and $R_2 = 6 \text{ cm}$. Black lines represent isotherms. The temperatures of cold source (left boundary) and hot source (right boundary) are set at 283 and 313 K, respectively. The thermal conductivities of (a) reference (all areas) and (b) reference shell (Area II) are set to be the same, i.e., $222.5 \text{ W m}^{-1} \text{ K}^{-1}$. The thermal conductivities of sensor (Area I) and background (Area III) in (b)-(d) are set to be 108.2 and $222.5 \text{ W m}^{-1} \text{ K}^{-1}$, respectively. The thermal conductivities of (c) isotropic shell and (d) anisotropic metashell are 277.3 and $\begin{pmatrix} 178.0 & 0 \\ 0 & 349.0 \end{pmatrix} \text{ W m}^{-1} \text{ K}^{-1}$, respectively.

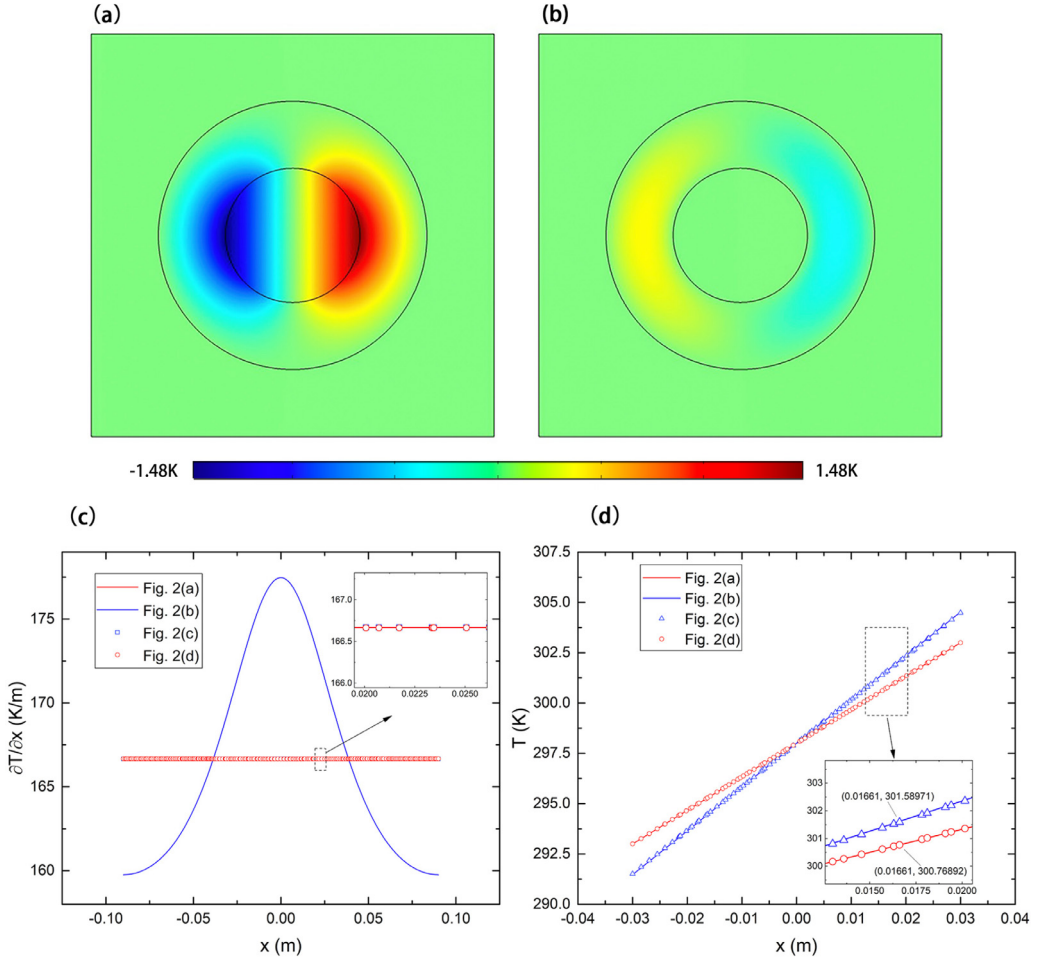


Fig. 3. Quantitative comparison of Fig. 2. Temperature-difference distributions with (a) the temperature in Fig. 2(c) minus that in Fig. 2(a) and (b) the temperature in Fig. 2(d) minus that in Fig. 2(a). (c) Temperature-gradient distributions on Line 1 in Fig. 2. (d) Temperature distributions on Line 2 in Fig. 2.

of temperature and normal heat flux,

$$\begin{cases} T_1(R_1) = T_2(R_1), \\ T_2(R_2) = T_3(R_2), \\ \left(-\kappa_1 \frac{\partial T_1}{\partial r} \right)_{R_1} = \left(-\kappa_{rr} \frac{\partial T_2}{\partial r} \right)_{R_1}, \\ \left(-\kappa_{rr} \frac{\partial T_2}{\partial r} \right)_{R_2} = \left(-\kappa_3 \frac{\partial T_3}{\partial r} \right)_{R_2}. \end{cases} \quad (4)$$

Considering the symmetry of boundary conditions, we only keep certain terms in Eq. (3) as the temperature profiles of three areas,

$$T_1 = A_0 + Ar \cos \theta, \quad (5)$$

$$T_2 = A_0 + Br^{m_1} \cos \theta + Cr^{m_2} \cos \theta, \quad (6)$$

$$T_3 = A_0 + Dr \cos \theta + Er^{-1} \cos \theta, \quad (7)$$

where the temperature at $\theta = \pm\pi/2$ is defined as A_0 , and $D = |\nabla T_0|$ is the modulus of an external linear thermal field ∇T_0 .

We have six undetermined coefficients (i.e., A , B , C , E , κ_{rr} , and $\kappa_{\theta\theta}$) and only four equations [Eq. (4)]. The other two equations are to make thermal sensors accurate and thermally invisible,

$$\begin{cases} A = D, \\ E = 0, \end{cases} \quad (8)$$

where $A = D$ indicates that the local temperature profile is the same as the background temperature profile, making a thermal sensor accurate; and $E = 0$ indicates that the background temperature profile is undistorted, making a thermal sensor invisible.

Then, the six unknown coefficients can be uniquely determined by six equations [Eqs. (4) and (8)], including the anisotropic thermal conductivity of the metashell $\kappa_2 = \begin{pmatrix} \kappa_{rr} & 0 \\ 0 & \kappa_{\theta\theta} \end{pmatrix}$. Therefore, thermal sensors with accuracy and thermal invisibility in two dimensions are designed.

On the same footing, we extend the two-dimensional theory to three dimensions. Accordingly, the thermal conductivity of the metashell is denoted as $\kappa_2 = \begin{pmatrix} \kappa_{rr} & 0 & 0 \\ 0 & \kappa_{\theta\theta} & 0 \\ 0 & 0 & \kappa_{\varphi\varphi} \end{pmatrix}$ with $\kappa_{\theta\theta} = \kappa_{\varphi\varphi}$. Then, Eq. (1) can be expanded in spherical coordinates (r, θ, φ) as

$$\frac{1}{r^2} \frac{\partial}{\partial r} \left(r^2 \kappa_{rr} \frac{\partial T}{\partial r} \right) + \frac{1}{r \sin \theta} \frac{\partial}{\partial \theta} \left(\sin \theta \kappa_{\theta\theta} \frac{\partial T}{\partial \theta} \right) = 0, \quad (9)$$

where φ is neglected because we consider a rotational symmetric case.

The general solution to Eq. (9) is

$$T = \sum_{i=0}^{\infty} (A_i r^{s_1} + B_i r^{s_2}) P_i(\cos \theta), \quad (10)$$

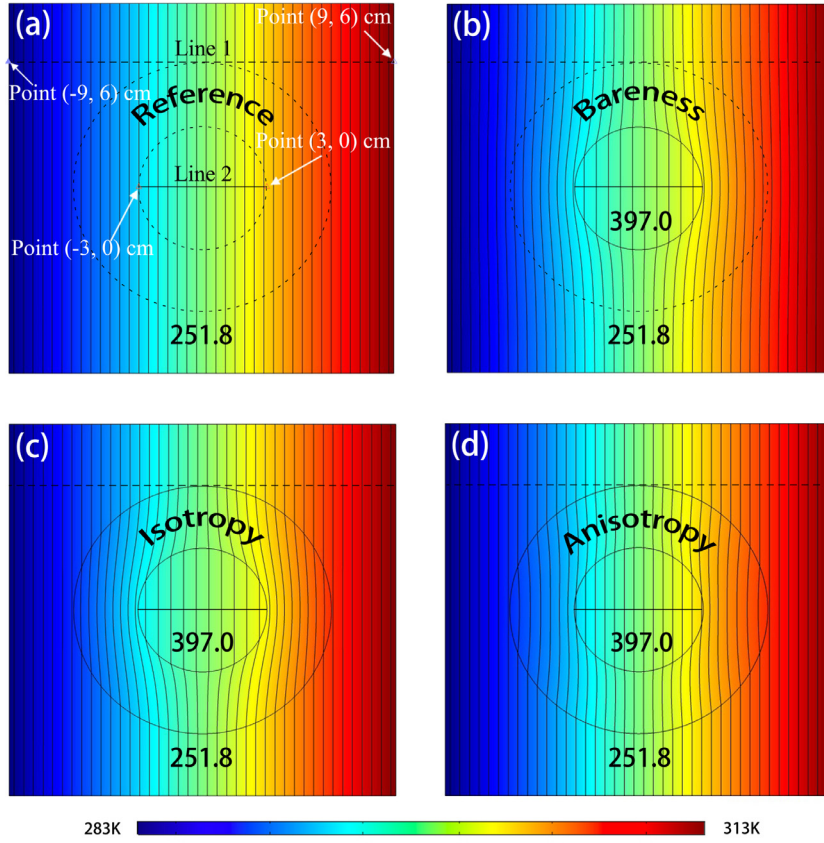


Fig. 4. Case with $\kappa_1 > \kappa_3$. The thermal conductivities of (a) reference (all areas) and (b) reference shell (Area II) are set to be the same, i.e., $251.8 \text{ W m}^{-1} \text{ K}^{-1}$. The thermal conductivities of sensor (Area I) and background (Area III) in (b)-(d) are set to be 397.0 and $251.8 \text{ W m}^{-1} \text{ K}^{-1}$, respectively. The thermal conductivities of (c) isotropic shell and (d) anisotropic metashell are 217.5 and $\begin{pmatrix} 308.0 & 0 \\ 0 & 104.0 \end{pmatrix} \text{ W m}^{-1} \text{ K}^{-1}$, respectively. Other parameters are the same as those for Fig. 2.

where $s_1 = \left[-1 + \sqrt{1 + 4i(i+1)\kappa_{\theta\theta}/\kappa_{rr}} \right]/2$, $s_2 = \left[-1 - \sqrt{1 + 4i(i+1)\kappa_{\theta\theta}/\kappa_{rr}} \right]/2$, i is summation index, and P_i is the Legendre polynomials. Since three-dimensional boundary conditions are the same as two-dimensional ones, the temperature profiles for three areas can be expressed as

$$T_1 = A_0 + Ar \cos \theta, \quad (11)$$

$$T_2 = A_0 + Br^{s_1} \cos \theta + Cr^{s_2} \cos \theta, \quad (12)$$

$$T_3 = A_0 + Dr \cos \theta + Er^{-2} \cos \theta, \quad (13)$$

where $s_1 = \left[-1 + \sqrt{1 + 8\kappa_{\theta\theta}/\kappa_{rr}} \right]/2$, $s_2 = \left[-1 - \sqrt{1 + 8\kappa_{\theta\theta}/\kappa_{rr}} \right]/2$, and the six unknown coefficients (i.e., A , B , C , E , κ_{rr} , and $\kappa_{\theta\theta}$) can also be solved by Eqs. (4) and (8). Therefore, we also make three-dimensional thermal sensors accurate and invisible. We use Mathematica to solve the six equations [Eqs. (4) and (8)] and obtain the required thermal conductivity of the metashell. Concrete expressions are presented in the Appendix.

3. Finite-element simulations

To confirm our theory, we further perform finite-element simulations with COMSOL MULTIPHYSICS [23]. For arbitrarily given thermal conductivities of backgrounds and sensors, we can derive

the anisotropic thermal conductivities of metashells and perform finite-element simulations.

For comparison, we present a reference with uniform thermal conductivity in Fig. 2(a). The finite-element simulations with a reference shell (a bare sensor embedded in the background, i.e., bareness), with an isotropic shell (calculated with theory in Ref. [9]), and with an anisotropic metashell (calculated by our theory) are presented in Fig. 2(b)–(d), respectively. Fig. 2(b) indicates that a bare thermal sensor indeed distorts local (Area I) and background (Area III) temperature profiles. Comparing Fig. 2(c) and (a), although the isotropic shell keeps the background temperature profile undistorted, the local temperature profile is still changed. Fortunately, our scheme [see Fig. 2(d)] makes local and background temperature profiles the same as those in Fig. 2(a), thus making the sensor accurate and thermally invisible.

To compare different schemes quantitatively, we also plot temperature-difference profiles with the temperature in Fig. 2(c) minus that in Fig. 2(a) [see Fig. 3(a)] and the temperature in Fig. 2(d) minus that in Fig. 2(a) [see Fig. 3(b)]. Clearly, the temperature difference in the local region of Fig. 3(a) is nonzero, indicating that the detected temperature is not the original one. Differently, the temperature difference in the local region of Fig. 3(b) is zero, making a thermal sensor accurate. Certainly, the temperature profile of the metashell has a small difference. We export the temperature-gradient distributions along x axis on Line 1 in Fig. 2, as shown in Fig. 3(c). The results indicate that the isotropic and anisotropic shells [see Fig. 2(c) and (d)] show the same advantage of thermal invisibility (i.e., the constant temperature-gradient distribution as that in reference). However, due to the thermal-

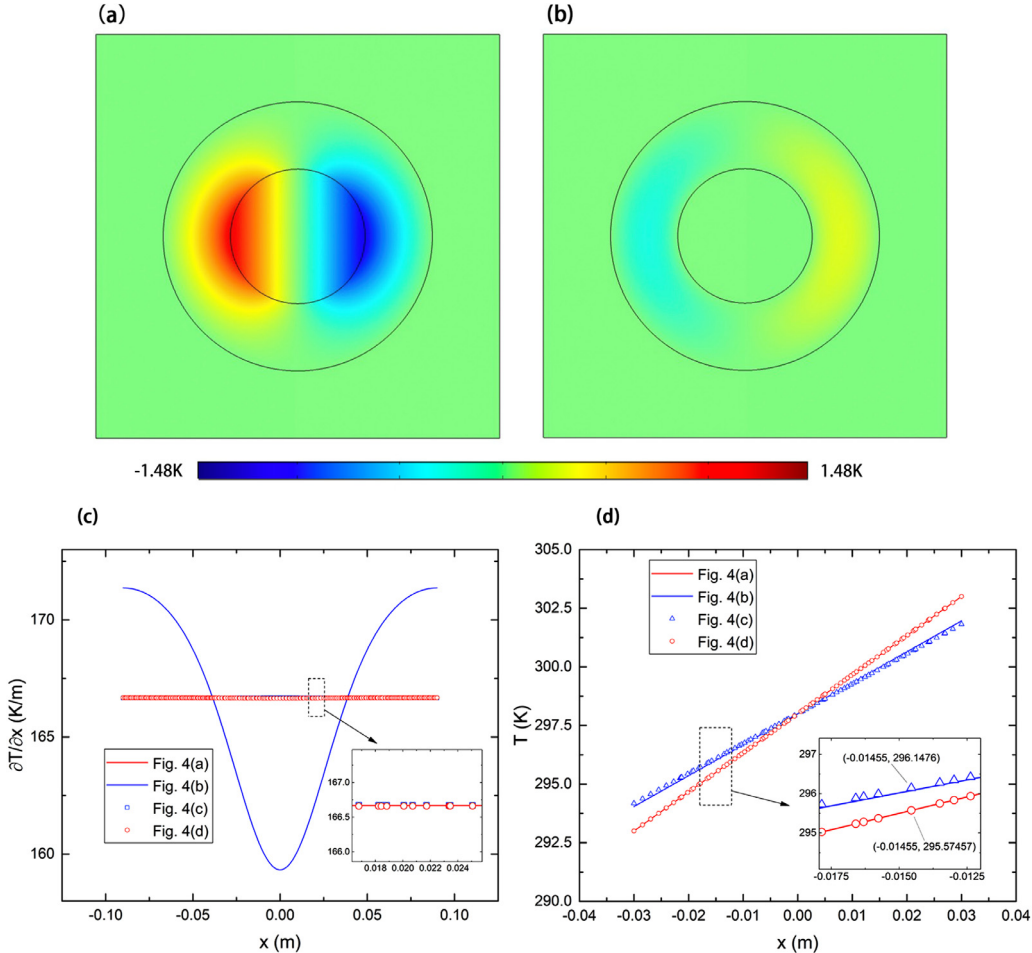


Fig. 5. Quantitative comparison of Fig. 4. Temperature-difference distributions with (a) the temperature in Fig. 4(c) minus that in Fig. 4(a) and (b) the temperature in Fig. 4(d) minus that in Fig. 4(a). (c) Temperature-gradient distributions on Line 1 in Fig. 4. (d) Temperature distribution on Line 2 in Fig. 4.

conductivity mismatch between the sensor and background, a bare sensor distorts the heat flow of original background thermal field, so the temperature gradient at the position of Line 1 in Fig. 2(b) is not a constant. We also export the temperature distributions on Line 2 in Fig. 2, as shown in Fig. 3(d). The results show that the anisotropic scheme is better than the isotropic one because what the thermal sensor in Fig. 2(d) detects is completely consistent with the reference. However, the detection in Fig. 2(c) deviates from the reference.

Moreover, we also discuss the case that the thermal conductivity of sensor (Area I) is larger than that of background (Area III), in order to ensure completeness; see Figs. 4 and 5. Essentially, the results are similar to Figs. 2 and 3. That is, a bare thermal sensor will distort temperature profiles of all areas [see Fig. 4(b)]. The existing isotropic scheme can keep the background temperature profile undistorted, but the local one is changed [see Fig. 4(c)]. The present scheme can ensure both local and background temperature profiles undistorted [see Fig. 4(d)]. Concrete data can be found in Fig. 5, which confirms the superiority of our scheme quantitatively.

To go further, we also perform three-dimensional finite-element simulations. The temperature profiles in the sensor (Area I) in Fig. 6(b) and (c) are different from that in Fig. 6(a), which means that the sensor cannot accurately measure local temperature distributions. Fortunately, the temperature profiles in sensor (Area I) and background (Area III) in Fig. 6(d) are identical with those in Fig. 6(a). We also perform quantitative analyses on “accurate” and “invisible” properties of the sensor [see Fig. 6(e)–(h)], and the results are exactly what we expect, just like the two-

dimensional case. To sum up, accuracy and invisibility of three-dimensional thermal sensors are also confirmed by finite-element simulations.

4. Laboratory experiments

To experimentally validate the finite-element simulations in Fig. 2(b) and (d), we set up a device shown in Fig. 7(a). By utilizing laser cutting, we fabricate two samples [see Fig. 7(b) and (c)] based on ellipse-embedded structures [18]. The holes in Areas I and III are uniformly distributed with circular shape, which can ensure that the effective thermal conductivities are isotropic. Differently, the holes in Area II have anisotropic (elliptical) geometry, so the effective thermal conductivity is also anisotropic. Therefore, the perforated structure indeed follows the theory. To eliminate infrared reflection and thermal convection as much as possible, we also apply transparent plastic films and foamed plastic films (insulated materials) on the upper and lower surfaces of the two samples, respectively. Then, we measure the temperature profiles of these two samples with the infrared camera Flir E60. The measured results with a reference shell and with an anisotropic metashell are shown in Fig. 7(d) and (e), respectively. We also perform finite-element simulations based on these two samples, as shown in Fig. 7(f) and (g). Both finite-element simulations [Fig. 2(b) and (d), and Fig. 7(f) and (g)] and experiments [Fig. 7(d) and (e)] prove that with the present scheme, a thermal sensor does accurately detect the local temperature profile without disturbing the background thermal field.

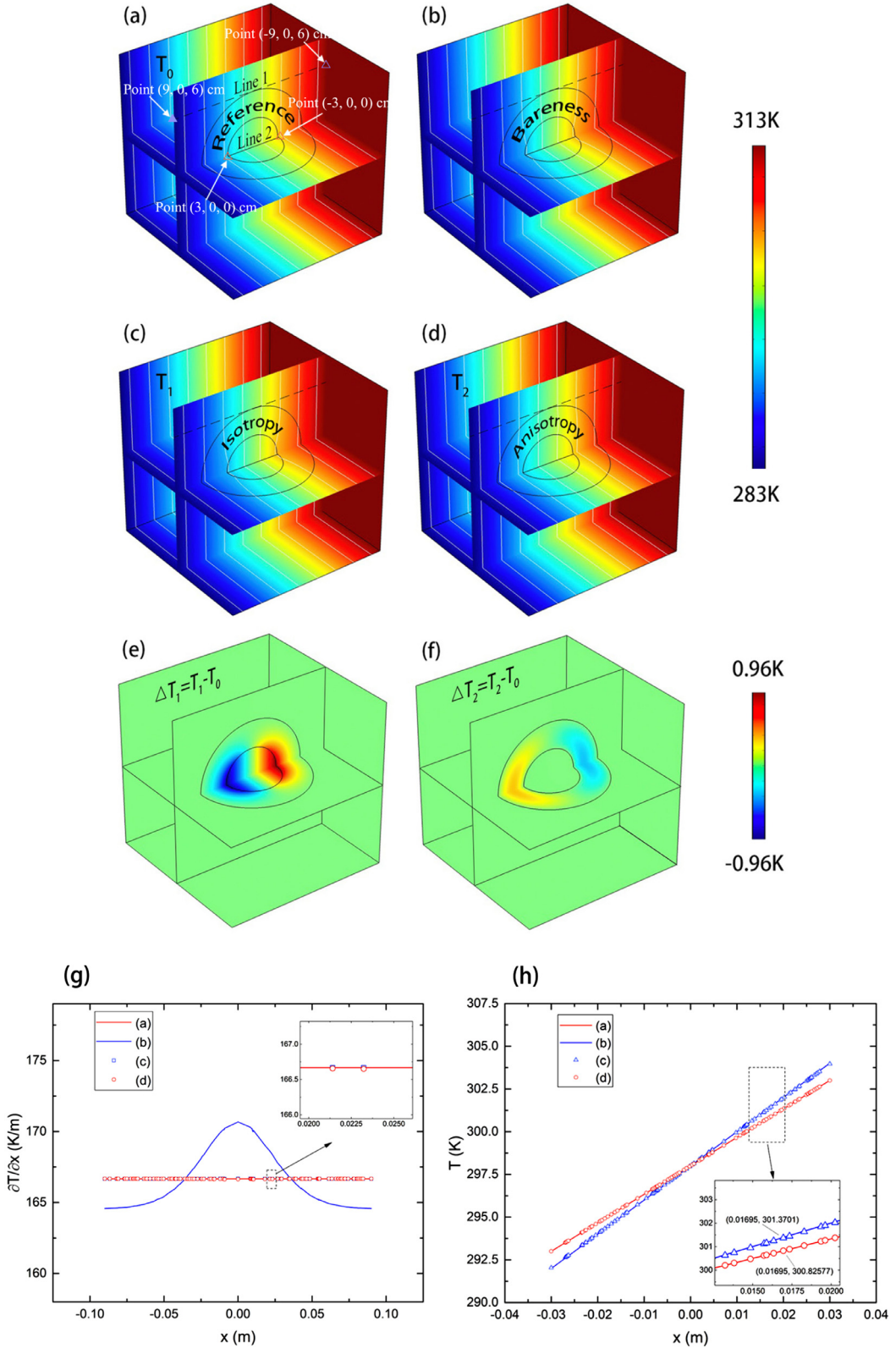


Fig. 6. Three-dimensional simulations. The simulation box is $18 \times 18 \times 18 \text{ cm}^3$, $R_1 = 3 \text{ cm}$, and $R_2 = 6 \text{ cm}$. The thermal conductivities of (a) reference (all areas) and (b) reference shell (Area II) are set to be the same, i.e., $222.5 \text{ W m}^{-1} \text{ K}^{-1}$. The thermal conductivities of sensor (Area I) and background (Area III) in (b)-(d) are set to be 108.2 and $222.5 \text{ W m}^{-1} \text{ K}^{-1}$, respectively. The thermal conductivities of (c) isotropic shell and (d) anisotropic metashell are 242.5 and $\begin{pmatrix} 183.7 & 0 & 0 \\ 0 & 269.0 & 0 \\ 0 & 0 & 269.0 \end{pmatrix} \text{ W m}^{-1} \text{ K}^{-1}$, respectively. Temperature-difference distributions with (e) the temperature in (c) minus that in (a) (i.e., $\Delta T_1 = T_1 - T_0$) and (f) the temperature in (d) minus that in (a) (i.e., $\Delta T_2 = T_2 - T_0$). (g) Temperature-gradient distributions on Line 1 in (a)-(d). (h) Temperature distributions on Line 2 in (a)-(d).

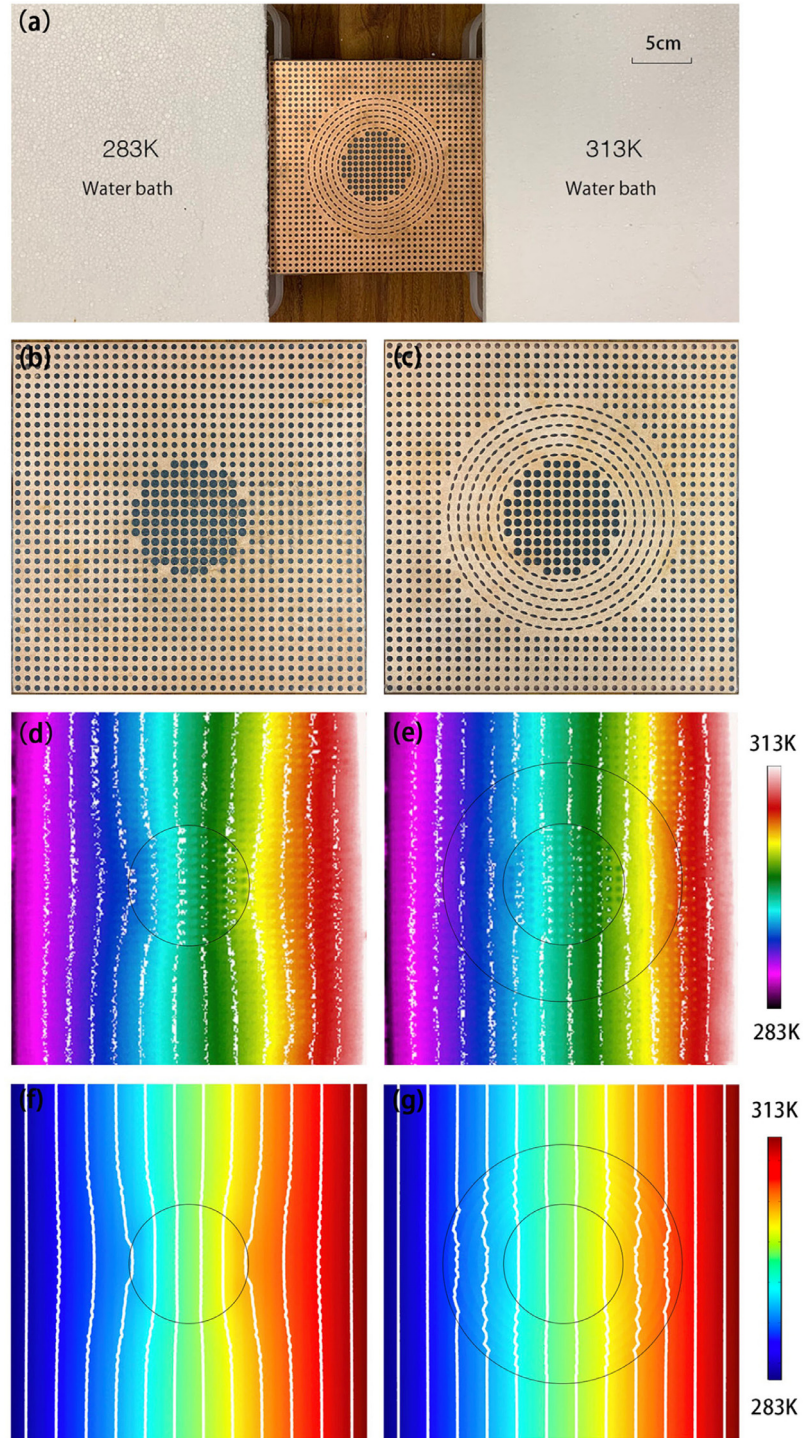


Fig. 7. Laboratory experiments. (a) Experimental setup. (b) and (c) Real photos of two samples. (d) and (e) [or (f) and (g)] are measured results (or finite-element simulations) corresponding to the two samples shown in (b) and (c), respectively. White lines represent isotherms. The sensor (or background) in (b) and (c) is carved with air circles with radius 0.21 cm (or 0.15 cm). The anisotropic metashell is carved with air ellipses with major (or minor) semiaxis of 0.21 cm (or 0.044 cm). The thermal conductivities of copper and air are 397 and $0.026 \text{ W m}^{-1} \text{ K}^{-1}$, respectively. These parameters cause the tensorial thermal conductivity of the anisotropic metashell in (c) to be $\begin{pmatrix} 178.0 & 0 \\ 0 & 349.0 \end{pmatrix} \text{ W m}^{-1} \text{ K}^{-1}$, and the thermal conductivities of sensor (or background) in (b) and (c) to be $108.2 \text{ W m}^{-1} \text{ K}^{-1}$ (or $222.5 \text{ W m}^{-1} \text{ K}^{-1}$). The sample size in (b) and (c) is the same as that for Fig. 2(b) and (d).

5. Discussion and conclusion

We have discussed the scheme in steady states, and it is also promising to extend the scheme to transient states by taking density and heat capacity into consideration. Furthermore, topology optimization is also a powerful method to design metamaterials [24–27] beyond transformation method [28–31], which may be applied to design accurate and invisible sensors.

In summary, we have proposed an anisotropic monolayer scheme to make thermal sensors accurate and thermally invisible. That is, by coating a thermal sensor with a metashell with anisotropic thermal conductivity, the thermal sensor can accurately measure local temperature profiles without disturbing surrounding thermal fields. The present scheme is validated by two-dimensional simulations and experiments, which is also applicable for three dimensions. These results may advance the performance of thermal detection and provide guidance to thermal camouflage [32–39]. On the same basis, this work also offers hints to obtain counterparts in other diffusive fields.

Declaration of Competing Interest

The authors declare that there are no conflicts of interest.

CRediT authorship contribution statement

Peng Jin: Formal analysis, Writing - original draft. **Liujun Xu:** Conceptualization, Writing - original draft. **Tao Jiang:** Writing - original draft. **Long Zhang:** Writing - original draft. **Jiping Huang:** Conceptualization, Writing - original draft.

Acknowledgment

We acknowledge financial support by the **National Natural Science Foundation of China** under Grant No. 11725521, and by the **Science and Technology Commission of Shanghai Municipality** under Grant No. 20JC1414700.

Appendix

Since κ_{rr} and $\kappa_{\theta\theta}$ appear in the exponent, it is difficult to analytically express them. To solve the problem, we treat κ_1 and κ_3 as two undetermined coefficients, which together with other coefficients can be respectively expressed in two and three dimensions as

$$\left\{ \begin{array}{l} A = |\nabla T_0|, \\ B = \frac{R_1^{m_2} R_2 - R_1 R_2^{m_2}}{R_1^{m_2} R_2^{m_1} - R_1^{m_1} R_2^{m_2}} |\nabla T_0|, \\ C = -\frac{R_1^{m_1} R_2 - R_1 R_2^{m_1}}{R_1^{m_2} R_2^{m_1} - R_1^{m_1} R_2^{m_2}} |\nabla T_0|, \\ E = 0, \\ \kappa_1 = \kappa_{rr} \frac{m_1 \left(-R_1^{m_1} R_2^{m_2} + R_1^{m_1+m_2-1} R_2 \right) + m_2 \left(R_1^{m_2} R_2^{m_1} - R_1^{m_1+m_2-1} R_2 \right)}{R_1^{m_2} R_2^{m_1} - R_1^{m_1} R_2^{m_2}}, \\ \kappa_3 = \kappa_{rr} \frac{m_1 \left(R_1^{m_2} R_2^{m_1} - R_1 R_2^{m_1+m_2-1} \right) + m_2 \left(-R_1^{m_1} R_2^{m_2} + R_1 R_2^{m_1+m_2-1} \right)}{R_1^{m_2} R_2^{m_1} - R_1^{m_1} R_2^{m_2}}, \end{array} \right. \quad (14)$$

$$\left\{ \begin{array}{l} A = |\nabla T_0|, \\ B = \frac{R_1^{s_2} R_2 - R_1 R_2^{s_2}}{R_1^{s_2} R_2^{s_1} - R_1^{s_1} R_2^{s_2}} |\nabla T_0|, \\ C = -\frac{R_1^{s_1} R_2 - R_1 R_2^{s_1}}{R_1^{s_2} R_2^{s_1} - R_1^{s_1} R_2^{s_2}} |\nabla T_0|, \\ E = 0, \\ \kappa_1 = \kappa_{rr} \frac{s_1 \left(-R_1^{s_1} R_2^{s_2} + R_1^{s_1+s_2-1} R_2 \right) + s_2 \left(R_1^{s_2} R_2^{s_1} - R_1^{s_1+s_2-1} R_2 \right)}{R_1^{s_2} R_2^{s_1} - R_1^{s_1} R_2^{s_2}}, \\ \kappa_3 = \kappa_{rr} \frac{s_1 \left(R_1^{s_2} R_2^{s_1} - R_1 R_2^{s_1+s_2-1} \right) + s_2 \left(-R_1^{s_1} R_2^{s_2} + R_1 R_2^{s_1+s_2-1} \right)}{R_1^{s_2} R_2^{s_1} - R_1^{s_1} R_2^{s_2}}, \end{array} \right. \quad (15)$$

Basically, Eqs. (14) and (15) have similar forms with only different $m_{1,2}$ and $s_{1,2}$.

References

- [1] A. Alù, N. Engheta, Cloaking a sensor, *Phys. Rev. Lett.* 102 (2009) 233901.
- [2] A. Greenleaf, Y. Kurylev, M. Lassas, G. Uhlmann, Cloaking a sensor via transformation optics, *Phys. Rev. E* 83 (2011) 016603.
- [3] R. Mach-Batlle, C. Navau, A. Sanchez, Invisible magnetic sensors, *Appl. Phys. Lett.* 112 (2018) 162406.
- [4] X.F. Zhu, B. Liang, W.W. Kan, X.Y. Zou, J.C. Cheng, Acoustic cloaking by a super-lens with single-negative materials, *Phys. Rev. Lett.* 106 (2011) 014301.
- [5] R. Fleury, J. Soric, A. Alù, Physical bounds on absorption and scattering for cloaked sensors, *Phys. Rev. B* 89 (2014) 045122.
- [6] R. Fleury, D. Sounas, A. Alù, An invisible acoustic sensor based on parity-time symmetry, *Nat. Commun.* 6 (2015) 5905.
- [7] X. He, L.Z. Wu, Thermal transparency with the concept of neutral inclusion, *Phys. Rev. E* 88 (2013) 033201.
- [8] X.Y. Shen, J.P. Huang, Thermally hiding an object inside a cloak with feeling, *Int. J. Heat Mass Transf.* 78 (2014) 1.
- [9] T.Z. Yang, X. Bai, D.L. Gao, L.Z. Wu, B.W. Li, J.T.L. Thong, C.W. Qiu, Invisible sensors: simultaneous sensing and camouflaging in multiphysical fields, *Adv. Mater.* 27 (2015) 7752.
- [10] T.Z. Yang, Y.S. Su, W.K. Xu, X.D. Yang, Transient thermal camouflage and heat signature control, *Appl. Phys. Lett.* 109 (2016) 121905.
- [11] T.C. Han, P. Yang, Y. Li, D.Y. Lei, B.W. Li, K. Hippalgaonkar, C.W. Qiu, Full-parameter omnidirectional thermal metadevices of anisotropic geometry, *Adv. Mater.* 30 (2018) 1804019.
- [12] T.C. Han, T. Yuan, B.W. Li, C.W. Qiu, Homogeneous thermal cloak with constant conductivity and tunable heat localization, *Sci. Rep.* 3 (2013) 1593.
- [13] T.Y. Chen, C.N. Weng, Y.L. Tsai, Materials with constant anisotropic conductivity as a thermal cloak or concentrator, *J. Appl. Phys.* 117 (2015) 054904.
- [14] R. Hu, S.Y. Huang, M. Wang, L.L. Zhou, X.Y. Peng, X.B. Luo, Binary thermal encoding by energy shielding and harvesting units, *Phys. Rev. Appl.* 10 (2018) 054032.
- [15] T.C. Han, J.J. Zhao, T. Yuan, D.Y. Lei, B.W. Li, C.W. Qiu, Theoretical realization of an ultra-efficient thermal-energy harvesting cell made of natural materials, *Energy Environ. Sci.* 6 (2013) 3537.
- [16] L.J. Xu, S. Yang, J.P. Huang, Passive metashells with adaptive thermal conductivities: chameleonlike behavior and its origin, *Phys. Rev. Appl.* 11 (2019) 054071.
- [17] L.J. Xu, J.P. Huang, Chameleonlike metashells in microfluidics: a passive approach to adaptive responses, *Sci. China Phys. Mech. Astron.* 63 (2020) 228711.
- [18] S. Yang, L.J. Xu, R.Z. Wang, J.P. Huang, Full control of heat transfer in single-particle structural materials, *Appl. Phys. Lett.* 111 (2017) 121908.
- [19] J. Shang, R.Z. Wang, C. Xin, G.L. Dai, J.P. Huang, Macroscopic networks of thermal conduction: failure tolerance and switching processes, *Int. J. Heat Mass Transf.* 121 (2018) 321.
- [20] L.J. Xu, S. Yang, J.P. Huang, Thermal transparency induced by periodic interparticle interaction, *Phys. Rev. Appl.* 11 (2019) 034056.
- [21] J.X. Li, Y. Li, T.L. Li, W.Y. Wang, L.Q. Li, C.W. Qiu, Doublet thermal metadevice, *Phys. Rev. Appl.* 11 (2019) 044021.
- [22] G.L. Dai, J.P. Huang, Nonlinear thermal conductivity of periodic composites, *Int. J. Heat Mass Transf.* 147 (2020) 118917.
- [23] <http://www.comsol.com/>.
- [24] G. Fujii, Y. Akimoto, M. Takahashi, Exploring optimal topology of thermal cloaks by CMA-ES, *Appl. Phys. Lett.* 112 (2018) 061108.
- [25] G. Fujii, Y. Akimoto, Optimizing the structural topology of bifunctional invisible cloak manipulating heat flux and direct current, *Appl. Phys. Lett.* 115 (2019) 174101.
- [26] G. Fujii, Y. Akimoto, Topology-optimized thermal carpet cloak expressed by an immersed-boundary level-set method via a covariance matrix adaptation evolution strategy, *Int. J. Heat Mass Transf.* 137 (2019) 1312.
- [27] G. Fujii, Y. Akimoto, Cloaking a concentrator in thermal conduction via topology optimization, *Int. J. Heat Mass Transf.* 159 (2020) 120082.
- [28] C.Z. Fan, Y. Gao, J.P. Huang, Shaped graded materials with an apparent negative thermal conductivity, *Appl. Phys. Lett.* 92 (2008) 251907.
- [29] T.Y. Chen, C.N. Weng, J.S. Chen, Cloak for curvilinearly anisotropic media in conduction, *Appl. Phys. Lett.* 93 (2008) 114103.
- [30] L.J. Xu, G.L. Dai, J.P. Huang, Transformation multithermatics: controlling radiation and conduction simultaneously, *Phys. Rev. Appl.* 13 (2020) 024063.
- [31] L.J. Xu, S. Yang, G.L. Dai, J.P. Huang, Transformation omnithermatics: simultaneous manipulation of three basic modes of heat transfer, *ES Energy Environ.* 7 (2020) 65.
- [32] Y. Li, X. Bai, T.Z. Yang, H. Luo, C.W. Qiu, Structured thermal surface for radiative camouflage, *Nat. Commun.* 9 (2018) 273.
- [33] R. Hu, S.L. Zhou, Y. Li, D.Y. Lei, X.B. Luo, C.W. Qiu, Illusion thermotics, *Adv. Mater.* 30 (2018) 1707237.
- [34] S.L. Zhou, R. Hu, X.B. Luo, Thermal illusion with twinborn-like heat signatures, *Int. J. Heat Mass Transf.* 127 (2018) 607.
- [35] J. Guo, Z.G. Qu, Thermal cloak with adaptive heat source to proactively manipulate temperature field in heat conduction process, *Int. J. Heat Mass Transf.* 127 (2018) 1212.

- [36] R. Hu, S.Y. Huang, M. Wang, X.L. Luo, J. Shiomi, C.W. Qiu, Encrypted thermal printing with regionalization transformation, *Adv. Mater.* 31 (2019) 1807849.
- [37] J. Qin, W. Luo, P. Yang, B. Wang, T. Deng, T.C. Han, Experimental demonstration of irregular thermal carpet cloaks with natural bulk material, *Int. J. Heat Mass Transf.* 141 (2019) 487.
- [38] L.J. Xu, S. Yang, J.P. Huang, Dipole-assisted thermotics: experimental demonstration of dipole-driven thermal invisibility, *Phys. Rev. E* 100 (2019) 062108.
- [39] X.Y. Peng, R. Hu, Three-dimensional illusion thermotics with separated thermal illusions, *ES Energy Environ.* 6 (2019) 39.